Biosensors and Bioelectronics 127 (2019) 19–24

Contents lists available at ScienceDirect

Biosensors and Bioelectronics

journal homepage: www.elsevier.com/locate/bios

A novel micromachined Fabry-Perot interferometer integrating nano-holes and dielectrophoresis for enhanced biochemical sensing

Long Tu[a,b], Liang Huang[a], Wenhui Wang[a,*]

[a] State Key Laboratory of Precision Measurement Technology and Instrument, Department of Precision Instrument, Tsinghua University, Beijing, China
[b] National Innovation Institute of Defense Technology, Beijing, China

ARTICLE INFO

Keywords:
Nano-hole
Extraordinary optical transmission (EOT)
Fabry–Perot microcavity
Dielectrophoresis (DEP)
Biochemical sensor

ABSTRACT

Single-layered gold nano-hole arrays lead to extraordinary optical transmission (EOT)-modulated surface plasmonic resonance (SPR) and have seen much progress in biochemical sensing. To further improve the sensing performance, the single-layered structure need to be changed. In this paper, a micromachined Fabry-Perot interferometer (μFPI), featuring two parallel and flat gold-coated mirrors, one of which has sub-wavelength nano-hole arrays, was designed, fabricated, and tested experimentally. Its transmission spectrum was confirmed to have EOT-modulated SPR patterns, and its characteristic peak wavelength was found to have a refractive index sensitivity of 593 nm / RIU and a Q factor up to 128.4, which is 10.2 times its EOT counterparts. By applying AC electric signals across the two gold layers, dielectrophoresis (DEP) induced near the nano-holes was proven to enrich particles significantly. To remove the thermal effects on the transmission spectrum, heat was dissipated by flowing sample during measurement. Biochemical sensing experiments were conducted using BSA protein medium of different low concentrations, demonstrating the detection sensitivity enhancement of ~ 6-fold for 1 pM compared to 100 pM. This novel μFPI presents a new paradigm in EOT-based SPR sensing technology by combining the benefits of μFPI interference, EOT near-field measurement and DEP enrichment of molecules.

1. Introduction

Single-layered nano-hole array perforated noble metal film can induce extraordinary optical transmission (EOT), which was discovered in 1998 (Ebbesen et al., 1998) and has been well attempted for SPR-like near-field biochemical sensing applications. When there is a change to the refractive index (RI) of medium in the near-field distance (i.e., 200 nm) of the nano-holes, the EOT transmission spectrum exhibits a shift in the peak wavelength. Normally this RI change correlates with the wavelength shift in a linear manner, and biochemical molecules combining with the nano-holes would cause such RI change. This sensing principle lends such single-layered nano-hole devices capability of label-free sensing the concentration for a range of biochemical species, including proteins (Im et al., 2010; Menezes et al., 2010), chemicals (Valsecchi and Brolo, 2013), etc. Because of their miniaturization nature, nano-hole EOT array devices have the special advantage of integrating with microfluidics to form lab-on-a-chip detection platforms (Tu et al., 2017), making EOT-based biochemical sensing techniques appealing.

Compared with other biochemical detection technologies, such as spectroscopic analysis technology, electrochemical analysis technology, electrophoresis technology, chromatography technology, and centrifugal technology, EOT-based technology has the characteristics of label-free, real-time, high-sensitivity and small-damage to the detection object (Xu et al., 2018; Chinnadayyala et al., 2018; Vashist et al., 2015; Sharma et al., 2018). Its unique advantages include that the spatial resolution is higher, the detection ability of small molecules is stronger, and the resonance peak wavelength can be tuned by the structure of the nano-hole array (Singh, 2016). Compared to the traditional and mature Kretschmann prism SPR configuration, EOT nano-holes have been recently advancing extensively to improve the sensing performance. Efforts have been made in the category of nano-hole geometry (shape, aspect ratio) (van der Molen et al., 2005; Koerkamp et al., 2004), array topology (Degiron et al., 2004; Rodrigo et al., 2010), structure (Thio et al., 2001; Lezec et al., 2002), fabrication process (Lesuffleur et al., 2009), material (Rodrigo et al., 2008, 2009), optical signal acquisition and processing (Najiminaini et al., 2010). For example, the double-hole geometry was tried (Lesuffleur et al., 2007) and found to increase the sensitivity by 50% to 600 nm / RIU. Also, complicated optical setup and laser source was used (Stark et al., 2005), in which the transmission light intensity and the reference light intensity were both recorded and used for measurement. It was shown that EOT-based sensing could

* Corresponding author.
E-mail address: wwh@tsinghua.edu.cn (W. Wang).

https://doi.org/10.1016/j.bios.2018.12.013
Received 18 September 2018; Received in revised form 9 December 2018; Accepted 10 December 2018
Available online 13 December 2018
0956-5663/ © 2018 Elsevier B.V. All rights reserved.

outperform the prism-based and grating-based SPR sensing methods in sensitivity by 6–20 fold. Flow-through nano-holes (Gordon et al., 2008) were proposed, and it was found that the measurement response was improved by tens of folds, due to the analyte enrichment through the nano-holes (Tu et al., 2015). The moving-average method (Najiminaini et al., 2012) was proposed to denoise the signal and the limit of detection reached 200 pM–40 nM. Also, a multiple-polarization spectral integration method (Lee et al., 2012) was proposed to improve the sensitivity and the limit of detection was improved by 8 times. All these valuable methods could be readily applied to single-layered nano-hole array structure. However, it is important to think further. What if the single-layered nano-hole array structure would have reached its limit in sensing performance?

Recently reported (Sharma et al., 2018) was a nanostructured micromachined Fabry-Perot interferometer (μFPI), which embedded one layer of gold-coated nanopores in its 50 μm cavity. The structure offers several advantages over a traditional μFPI for label-free biosensing applications, including increased sensing surface area, extended penetration depth of the excitation light and amplified optical transducing signals. As a result, the biosensing performance indicators like free spectral range, finesse, and contrast of optical transducing signals were increased significantly. This nanostructured μFPI showed great potential. However, as the authors indicate, the structure can be optimized further for enhanced performance. (i) One side of the μFPI is PDMS, which does not have good reflection as the metal layer of a classic μFPI. Plus, its surface deformation caused by microfluidic flowing may affect the interference patterns. (ii) The other side of the μFPI is 3 μm AAO (anodic aluminium oxide), which has irregularly arrayed and shaped nanopores. This may deteriorate the EOT effect and limit the performance. (iii) The transducing signals are interference light reflected from the AAO. Thus, the incident light and reflecting light are on the same side of the device, which may complicate the measurement setup.

Inspired from the μFPI concept, therefore, in this paper, we propose to construct a μFPI by two parallel gold-coated glass slides as mirrors. One mirror has only one thin and even layer of sputtered gold; the other also has one thin and even layer of sputtered gold but is perforated with nano-holes, serving as the EOT-signal modulator to amplify transmission signals at resonant wavelengths. Since the μFPI cavity has two gold-coated mirrors, an electric signal could be applied to generate electrophoresis or dielectrophoresis (DEP), which could enrich particles in measurement process like the reported work (Escobedo et al., 2012). Combining with microfluidics, the μFPI cavity could be configured as the microfluidic channel, where the analytes can be easily handled on-chip and ample fluidic means can be applied for different purposes, for example, here to overcome heating problems related to measurement environment. Collectively, the Q factor and sensitivity were improved significantly.

2. Materials and methods

2.1. Concept, design and fabrication of the μFPI with nano-holes

As shown in Fig. 1, the μFPI has two mirrors, each of which has a thin and even layer of sputtered gold. The two gold layers facing each other in parallel inside the microcavity, whose length (distance between the two mirrors) is determined by microchannel-patterned spacer. One of the gold layers (the lower layer) has an array of nano-holes with a sub-wavelength diameter (i.e., 200 nm). Two through holes are formed in the upper glass as inlet and outlet for sample loading and waste collecting. A straight microchannel above the nano-hole sensing hotspots is patterned on the spacer to allow the fluidic sample flowing over. The gold layers coated on the two separate mirrors can be wired to an external power source to provide an electric field for electrophoresis or DEP, which functions to enrich analytes in the vicinity of the nano-holes. The device is operated under transmission mode, i.e., the incident light is normally projected from one side of the microcavity, while the transmission light is collected from the other side for sensing purpose.

The thickness of the upper gold layer is chosen to be 20 nm, less than the skin depth of gold, which is about 70 nm, to allow strong enough transmission signal to be collected. Using FDTD (finite-different time-domain) simulation method, we fixed the parameters for the lower nano-hole gold layer but changed the thickness of the upper gold layer from 10 nm to 50 nm at 10 nm interval. We found that the transmittance of the interference peak decreases with the thickness. In principle, 10 nm thickness for the upper gold film is the best. In practice, however, limited by our fabrication procedure, we obtained 20 nm thickness for the upper gold film stably in this study. This is acceptable because the transmittance for the thickness of 20 nm is up to 10 times that for 50 nm according to the simulation results (Fig. S1). This thickness was also proven workable in experiment.

Subsequently, the influence of μFPI cavity length (the spacing between the two mirrors) on transmission spectrum is calculated by FDTD simulations. With the thickness of the upper gold film fixed at 20 nm, we simulated the transmission spectrum for cavity length of 5 μm, 10 μm, 20 μm, and 30 μm respectively. The transmittance spectral results are shown in Supporting information (Fig. S2).

Fabry-Perot theory (Formulas S1-S4) indicates that the smaller the cavity length, the greater the free spectral range. If we look into the free spectral range around 800 nm (Fig S2), its values rise from 8 nm for 30 μm to 43 nm for 5 μm. A smaller free spectral range means that a smaller wavelength interval need to be separated in the spectrum, which is inconvenient for spectrum identification. In particular, when the free spectral range is less than the potential wavelength shift in real detection, the peak wavelength may be wrongly picked. Therefore, to ensure a rather big free spectral range, the smaller the cavity length, the better. However, in actual detection application, if the cavity length is too small, it would need extra efforts in handling solution to be detected. For example, the flow resistance becomes greater for smaller cavity length. In particular, the flow resistance is inversely proportional to the cubic of the cavity length (Bruus, 2008), in consideration of the microchannel dimension (3 mm wide, 12 mm long) formed in the μFPI cavity. Thus, without loss of generality, the μFPI cavity length was set to be 10 μm in this study. This resulted in a flow resistance of 10 Pa·min/μL level, which facilitated our device fabrication in bonding and microfluidic experiment in pumping.

The two layers were fabricated separately and then assembled, as shown in Fig. 2. Resembling the standard FIB fabrication process of

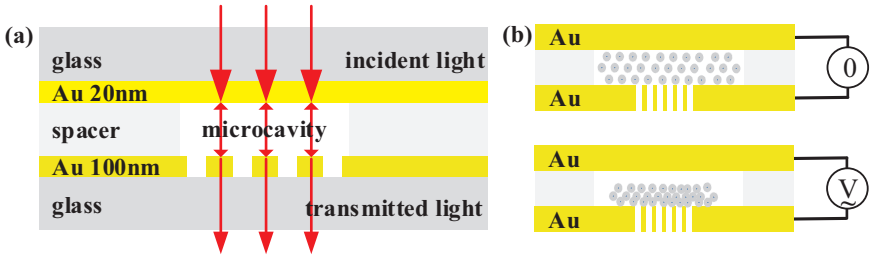

Fig. 1. Schematic of the μFPI. (a) Basic structure. (b) DEP enrichment concept.

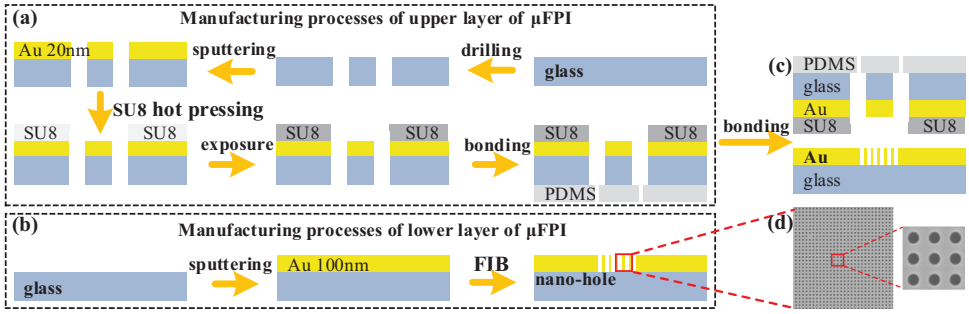

Fig. 2. Fabrication procedure of the μFPI. (a)Manufacturing processes of upper μFPI. (b) Manufacturing processes of lower μFPI. (c) Schematic diagram of assembling upper and lower μFPI into a total μFPI. (d) SEM of nano-hole array on lower layers of μFPI, with period of 500 nm.

nano-holes (Dhawan et al., 2008), the lower layer starts from a glass slide, which is thoroughly washed and dried for gold film sputtering. A 5 nm thick chromium layer is firstly sputtered on the glass slide as the seeding layer, then a 100 nm thick gold film is sputtered. Subsequently, a specific nano-hole region of the gold film is perforated by FIB with nano-holes of 200 nm in diameter. These nano-holes are configured into a matrix of 80 × 80, collectively covering a footprint of ~ 40 μm × 40 μm, with a period of 500 nm.

The upper layer also starts from a glass slide, which is drilled to have two round through holes of 3 mm in diameter and 12 mm in distance as the inlet and outlet. The glass slide is then washed thoroughly and dried for sputtering 5 nm thick chromium film and subsequently 15 nm thick gold film. Next, a 10 μm thick SU-8 dry film (purchased from Suzhou Ruicai Corporation) is bonded to the glass substrate by a laminator through thermocompression at 100 °C. The SU-8 dry film was then subject to soft lithography to form the microchannel, inlet and outlet. Finally, the other side of the glass slide is bonded with a bulk of PDMS, which is punched to have the inlet and outlet ports connecting to the through-mirror inlet and outlet.

Once having the two layers, we sandwich them together with two ring-shaped (central holed) permanent magnets on the two sides of the μFPI. The ring magnets allow flexible assembly / disassembly of the device, and the central holes permit fluidic tubing and unblocked optical path. Note, to facilitate electrode wiring, the two glass slides have different size.

2.2. Interference phenomenon observation of F-P microcavity nano-hole array

To compare the spectra of single-layered EOT nano-holes and μFPI, the μFPI was disassembled and assembled for two experiments. To get the single-layered EOT signal, the lower layer having the single-layered EOT nano-holes of the μFPI was disassembled and immersed in DI water. To get the μFPI signal, the μFPI was then assembled and filled with DI water in its cavity. For both cases, the transmission spectrum was recorded and shown in Fig. 3. It can be seen that the transmission spectrum of the μFPI is equivalent to the multiple-beam interference spectrum modulated by the EOT transmission spectrum of the single-layered gold nano-hole array. The interference effect is paramount indicated by the interference contrast for the interference peak at 752 nm. The interference contrast reaches 0.9, calculated by $(I_{max}\text{-}I_{min})$ / $(I_{max}+I_{min})$, where I_{max} and I_{min} are the maximum and minimum values of the light intensity in the interference spectrum.

The free spectral range between two adjacent interference peaks observed from the experiment is in agreement with the theoretical value. The expression of free spectral range is given by λ_k^2 / $(2nL)$, where λ_k is the kth-level interference pattern wavelength, n is the RI of the medium in the μFPI, and L is the μFPI cavity length. Taking the interference peak at 752 nm for example, the theoretical value of the free spectral range is 21.2 nm (n = 1.333, L = 10 μm), while the measured value is 18.8 nm. The deviation w.r.t. the theoretical value is 11%, which is reasonable considering the nano fabrication process would not be perfect. Notably, it can be seen from the figure that the full width at half maximum (FWHM) of the interference peak is greatly decreased compared with the single-layered nano-holes. The FWHM of the interference peak at 752 nm is 4.6 nm, while the FWHM of the corresponding single-layered gold nano-holes is 48.2 nm. This 10 times reduction in FWHM indicates 10 times increase in signal to noise ratio (SNR).

2.3. Selection of interference peaks in sensing measurements

There is some tradeoff in selecting which interference peak among many as the characteristic peak in wavelength shift measurement. Theoretically, the RI sensitivity is given by λ_k / n, which means the longer the wavelength, the greater the sensitivity. Thus, we should always choose the wavelength in the right end of the EOT spectrum. Coincidently, the signal for analytes to be measured actually stays in the right end (Fig. 3a). So this would be no problem. In addition, to allow a better SNR, the interference peak with the highest intensity would be ideal. Furthermore, we have to choose the wavelength within the range of our spectrometer. Therefore, collectively, the interference peak at 752 nm was selected as the characteristic peak in this study.

2.4. Materials

In this study, deionized (DI) water (conductivity 0.95 μS/cm), saline of different concentrations (1%, 5%, 10%, 15%, 20%, 25%), and BSA (molecular weight: 65 kDa, Sigma-Aldrich) solution of four low concentrations (0 pM = DI water, 1 pM, 10 pM, and 100 pM) were used.

3. Experimental

3.1. Experimental setup

The experimental setup is mainly based on a standard inverted microscope (Nikon, TE2000), as shown in Supporting information (Fig. S3). The optical setup is as follows: the filtered white light radiated from tungsten-halogen lamp is illuminating the nano-hole array from above. The microscopic imaging system converges the light on the imaging focal plane of a C-mount side port, which is connected to a fiber optic spectrometer (Ocean Optics QE65Pro) for spectrum measurement. One arbitrary waveform generator (Tektronix AFG3052C) is connected to the gold films of the μFPI to provide external electric fields. In particular, the lower gold layer is grounded and the upper layer is applied with sine waves to generate pDEP in the nano-hole sensing region. The volume flow rate is controlled by a syringe pump (Legato 200) using push-pull mode, which drives the flow in and out of the microchannel through the fluidic connectors (i.e., 10 μL/min). The experiment is conducted at room temperature (25 °C constant).

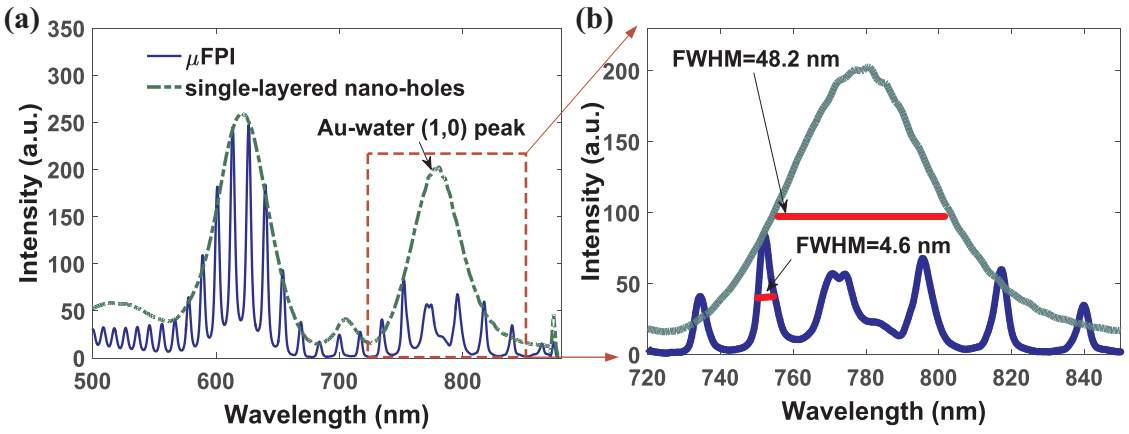

Fig. 3. Transmission spectrum for the μFPI and single-layered gold nano-hole arrays. (a) Transmission spectrum in the full measurable spectrum range. (b) Zoom-in view of the spectrum for gold-water interface.

3.2. Experimental design and procedures

The RI sensitivity of the interference peak at 752 nm was firstly obtained with pure water and saline of different concentrations. During experiment, the liquid with increasing concentrations was pumped into the μFPI and the corresponding peak wavelength around the characteristic wavelength was recorded through the spectrometer.

Thermal effects are a common problem to μFPI and plasmonic nano-holes. During measurement, the typical thermal effects may be attributed to such factors as the heat radiation of the light source or the joule-heating associated with DEP. The heat generated by both of them will increase the environment temperature in the μFPI microcavity and cause the RI of the medium to decrease (Xu et al., 2017). For example, the RI of water decreases by nearly 0.001 corresponding to 20 °C increase of temperature. Correspondingly, the signal baseline would suffer from a blue shift (i.e., the peak wavelength moves toward the short-wave direction in the spectrum). To verify this phenomenon and cancel the thermal effect, we conducted an experiment without DEP by using static and flowing DI water inside the μFPI cavity as a comparison, during which the spectral shift was recorded. The μFPI was first pumped with DI water for a total of 500 s at a flow rate of 10 μL/min. Then the microfluidic pump was completely stopped to keep the DI water stagnant till 2500 s, and finally turned on to restore the volume flow rate to 10 μL/min.

We finally used BSA solutions to demonstrate the utility of DEP-enhanced plasmonic sensing in detecting protein molecules of low concentrations. With reference to literature (Barik et al., 2014), the DEP frequency was set to be 1 MHz and the voltage peak-to-peak value = 1 V. In such case, pDEP will be generated to attract BSA molecules on the hotspots of the nano-holes. To demonstrate the DEP effect, experiments were performed without DEP for 500 s, followed by DEP for a longer period of 1250 s. To remove the heating effect, during the course of experiments, BSA solution was flowed through the μFPI at a flow rate of 10 μL/min. To test the reproducibility and overall error, five tests were performed with the same setting and the μFPI was thoroughly washed between each two tests.

4. Results and discussion

4.1. Refractive index sensitivity measurement

Fig. 4a exemplifies the transmission spectrum recorded for pure water, 10% and 25% concentration of salt water. The relationship between the peak wavelength and the RI for the 7 concentrations is linearly fitted, as shown in Fig. 4b. The RI sensitivity is S = 593 nm / RIU, and the theoretical value is calculated to be 564 nm / RIU (λ = 752 nm, n = 1.333). The deviation w.r.t. the theoretical value is 5.5%. In this case, the Q factor (S/FWHM) of the interference peak at 752 nm is calculated as 128.4, which is currently the highest in EOT nano-hole sensing structures.

Three performance indicators, including the RI sensitivity, interference contrast ratio and Q factor of the μFPI in this paper are compared with those of the typical single-layered nano-holes or μFPI, and summarized in Table 1. It can be seen that the RI sensitivity of the μFPI is at a high level compared to existing single-layered nano-hole structures, while the interference contrast ratio and the Q factor are the

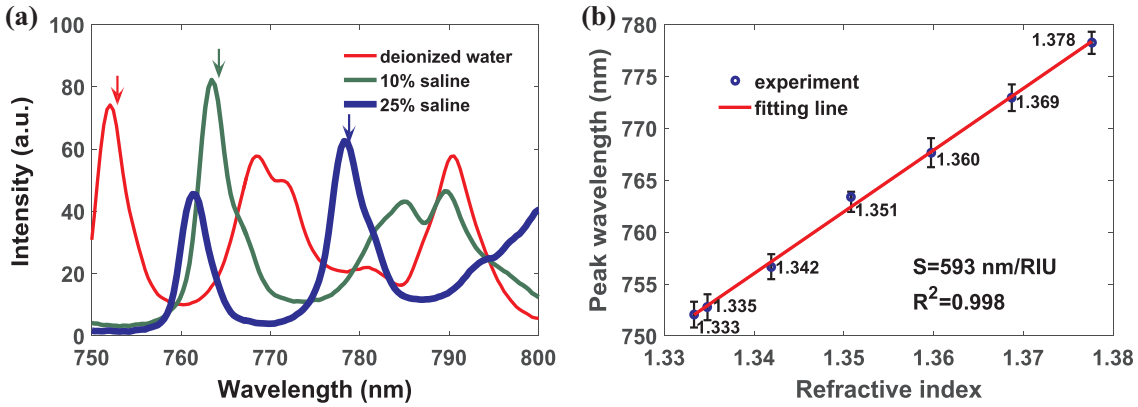

Fig. 4. RI sensitivity of the μFPI. (a) The spectrum in the gold-salt water range. (b) RI sensitivity curve. The refractive index n and the saline concentration w is obtained via n = 1.333 + 0.1783w (Haynes, 2014).

Table 1
Comparison of the performance indicators of the μFPI and typical single-layered or double-layered gold nano-hole arrays.

structure	research group	RI sensitivity	Interference contrast	Q factor
Single layer	Alexandre G. Brolo (De Leebeeck et al., 2007)	400 nm / RIU	None	None
Single layer	Alexandre G. Brolo ()	271 nm / RIU	None	11.7
Single layer	Sang-Hyun Oh (Si et al., 2012)	495 nm / RIU	None	50
Single layer	TW Odom (Henzie et al., 2007)	313 nm / RIU	None	23.3
Single layer	Hatice Altug (Yanik et al., 2010)	630 nm / RIU	None	None
Double layer	Long queue (Zhang et al., 2010)	None	0.52	None
Double layer	This paper	593 nm / RIU	0.9	128.4

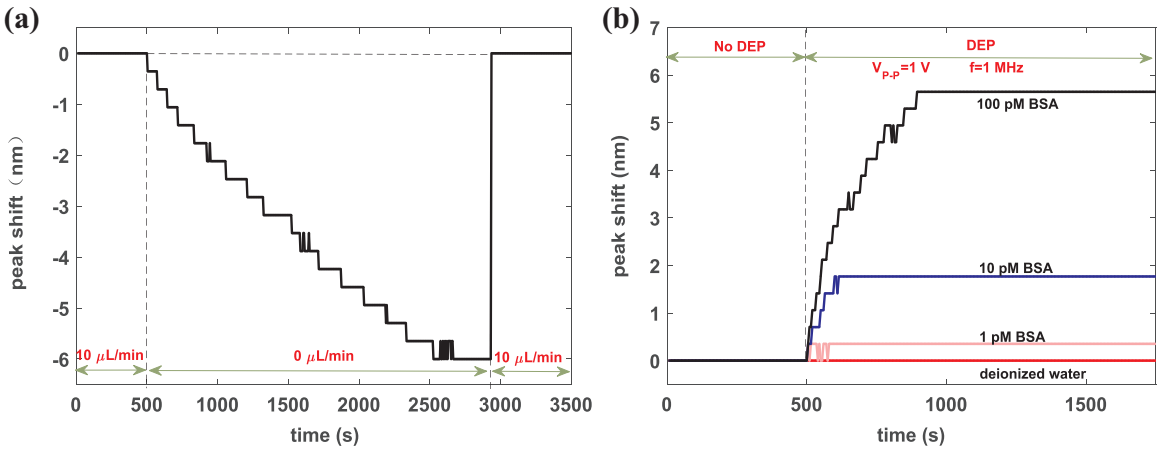

Fig. 5. Experimental results. (a) Dynamic shift in peak wavelength of the μFPI when DI water is stagnant or flowing in the microcavity. (b) Dynamic peak wavelength shift curve corresponding to different low-concentration BSA protein solutions with / without DEP.

highest in the field.

4.2. Verification and elimination of the thermal effect on μFPI signal

Fig. 5a shows the time-varying spectral shift throughout the experiment of flowing-stopping-reflowing the DI water. The spectral shift was observed stable or zero for the flowing period, to blue-shift dynamically and nearly stabilize at 2500 s for the stopping period, and immediately to reset to zero upon the onset of reflowing. From this experiment we could have two observations. Firstly, the thermal effect can affect the signal baseline significantly and dynamically. Secondly, to simply let the analyte sample flow can effectively eliminate the thermal effect. Though integrating some liquid-cooling microchannel above the sample flowing channel (Li et al., 2018) may work to remove the thermal effect, fabrication of the channel-on-channel structure is complicated. The experimental results prove that using dynamic flow to stabilize the environment temperature is applicable. Therefore, this simple and effective method was used in the BSA detection experiment and proved applicable as well.

Note in this work, we chose the flow rate of 10 μL/min such that for each spectral acquisition cycle the microchannel under illumination was totally exchanged with fresh fluid to take away potential heat. Generally, increasing the flow rate in the range of 0–10 μL/min would decrease the blue-shift till zero.

4.3. BSA concentration measurement enhanced by DEP

The time-varying spectral-shift curves for one typical test are shown in Fig. 5b. It can be seen from the figure that in the absence of DEP force (0–500 s), the spectral shift was zero for all the four low-concentration BSA solutions. This somehow testified that BSA protein adsorption on the gold nano-hole array by diffusion alone is not measurable. With DEP force (500–1750 s), the spectral shift remained unchanged as a control for DI water, because there is no BSA protein particle available for adsorption. In contrast, the spectral shift increased for BSA with increasing concentrations, e.g., 0.35 ± 0 nm for 1 pM, 1.77 ± 0 nm for 10 pM, and 5.65 ± 0 nm for 100 pM; and the time to measurement equilibrium was 78 ± 2.7 s, 111 ± 7.4 s and 419 ± 12.9 s, respectively, for the five tests. The measured spectral shift at equilibrium corresponding to each concentration was highly reproducible and consistent, while the time to measurement equilibrium had increasing error (indicated by the standard deviation) probably due to the randomness of the BSA molecule binding process. The DEP-assisted analyte enrichment effect was validated in agreement with the literature (Barik et al., 2014). Here, thanks to the μFPI sensing structure, the spectral shift was more pronounced than the literature (Barik et al., 2014), which would facilitate the selection of lower-resolution spectrometer.

Previously, researchers (Barik et al., 2014) already demonstrated the DEP-enhanced plasmonic sensing with gold nano-hole arrays. In that work, a stagnant droplet with analytes was sandwiched between an ITO glass and the nano-hole arrays to show the DEP working in concert with such effects as joule-heating-induced electrothermal flows or AC electroosmosis. These effects together facilitate the transport and subsequent capture of analyte molecules on the plasmonic hotspots of nano-holes. Here we used the same concept but taking advantage of the upper gold layer as one of the electrodes, instead of ITO glass.

By nature, EOT-based sensing is essentially only able to measure the change to refractive index, lacking the ability of selectivity of specific analytes. However, if the analytes have specific reaction with some species, the sensing scheme can be modified somehow like an antigen-antibody model in immunoassay to facilitate selectivity. For example, in (Im et al., 2012), the nano-hole surface could be coated with antigen, which was used to selectively bind and detect antibody.

However, from a larger view of point, compared with other biochemical detection technologies, EOT-based sensing method may not be the best in individual performance indicators. In terms of Q factor, for example, compared with their EOT counterparts, the performance was enhanced by ~10-fold, which is indeed a progress but not a great

breakthrough against other biochemical detection technologies. For real applications, the fabrication process looks relatively complex and need to be optimized.

5. Conclusions

In this paper, we present a novel nano-hole structured μFPI sensing scheme combining EOT-modulated multiple-beam interference and DEP. Through EOT-modulated interference, we realized a RI sensitivity of 593 nm/RIU and a Q factor up to 128.4, which is 10.2 times its EOT counterpart. Through DEP, we enhanced the detection sensitivity and assay time both by ~6-fold for 1 pM of BSA protein solution (e.g., 2.86 pM/nm, and 78 s) compared to 100 pM. The thermal effects caused by DEP were removed simply by flowing sample continually through the microcavity. For the future improvement, the specific binding and identification of molecules need to be considered, and the fabrication process should be more facile and cost-effective for real applications.

Acknowledgments

This work was supported by the National Key R&D Program (no. 2016YFC0900200), the NSFC (no. 61376120), and the One-Thousand Young Talent Program of China.

Conflict of interest

The authors declare no competing financial interest.

Credit author statement

Wenhui Wang conceived the study, obtained funding and resources, and supervised the project. Long Tu and Wenhui Wang participated in the entire experiment, designed experiment method, collected and analyzed data, and wrote the paper. Liang Huang made substantial contributions to the design of microchannel. All authors reviewed and approved the manuscript.

Appendix A. Supporting information

Supplementary data associated with this article can be found in the online version at doi:10.1016/j.bios.2018.12.013.

References

Yanik, A.A., et al., 2010. Integrated nanoplasmonic-nanofluidic biosensors with targeted delivery of analytes. Appl. Phys. Lett. 96 (2), 021101–021101-3.
Barik, A., et al., 2014. Dielectrophoresis-enhanced plasmonic sensing with gold nanohole arrays. Nano Lett. 14 (4), 2006–2012.
Degiron, A., et al., 2004. Optical transmission properties of a single subwavelength aperture in a real metal. Opt. Commun. 239 (1–3), 61–66.
De Leebeeck, A., Kumar, L.K.S., De Lange, V., et al., 2007. On-chip surface-based detection with nanohole arrays. Anal. Chem. 79 (11), 4094–4100.
Dhawan, A., et al., 2008. FIB fabrication of metallic nanostructures on end-faces of optical fibers for chemical sensing applications. J. Vac. Sci. Technol. B Microelectron. nanometer Struct.: Process. Meas. Phenom.: Off. J. Am. Vac. Soc. 26 (6), 2168–2173.
Sharma, A.K., Pandey, A.K., Kaur, B., 2018. A Review of advancements (2007–2017) in plasmonics-based optical fiber sensors. Opt. Fiber Technol. 43, 20–34.
Lesuffleur, A., et al., 2007. Periodic nanohole arrays with shape-enhanced plasmon resonance as real-time biosensors. Appl. Phys. Lett. 90 (24), 243110–243110-3.
Xu, B., et al., 2017. Hybrid Fabry-Perot interferometer for simultaneous liquid refractive index and temperature measurement. Opt. Express 25 (13), 14483–14493.
Escobedo, C., et al., 2012. Optofluidic concentration: plasmonic nanostructure as concentrator and sensor. Nano Lett. 12 (3), 1592–1596.
Valsecchi, C., Brolo, A.G., 2013. Periodic metallic nanostructures as plasmonic chemical sensors. Langmuir 29 (19), 5638–5649.
Bruus, H., 2008. Theoretical Microfluidics. Oxford University Press.
Im, H., et al., 2010. Membrane protein biosensing with plasmonic nanopore arrays and pore-spanning lipid membranes. Chem. Sci. 1 (6), 688–696.
Im, H., et al., 2012. Nanohole-based surface plasmon resonance instruments with improved spectral resolution quantify a broad range of antibody-ligand binding kinetics. Anal. Chem. 84 (4), 1941–1947.
Lezec, H.J., et al., 2002. Beaming light from a subwavelength aperture. Science 297 (5582), 820–822.
Si, H.L., et al., 2012. Linewidth-optimized extraordinary optical transmission in water with template-stripped metallic nanohole arrays. Adv. Funct. Mater. 22 (21), 4439–4446.
Henzie, J., Min, H.L., Odom, T.W., 2007. Multiscale patterning of plasmonic metamaterials. Nat. Nanotechnol. 2 (9), 549–554.
Menezes, J.W., et al., 2010. Large-area fabrication of periodic arrays of nanoholes in metal films and their application in biosensing and plasmonic-enhanced photovoltaics. Adv. Funct. Mater. 20 (22), 3918–3924.
Koerkamp, K.J.K., et al., 2004. Strong influence of hole shape on extraordinary transmission through periodic arrays of subwavelength holes. Phys. Rev. Lett. 92 (18).
Lee, K.-L., et al., 2012. Improving surface plasmon detection in gold nanostructures using a multi-polarization spectral integration method. Adv. Mater. 24 (35), OP253–OP259.
van der Molen, K.L., et al., 2005. Role of shape and localized resonances in extraordinary transmission through periodic arrays of subwavelength holes: experiment and theory. Phys. Rev. B 72 (4) (045421-045421-9).
Lesuffleur, A. et al. 2009. Plasmonic nanohole arrays for label-free kinetic biosensing in a lipid membrane environment. in: Proceedings of International Conference of the IEEE Engineering in Medicine & Biology Society.
Tu, Long, Huang, Liang, Wang, Wenhui, et al., 2015. Study of flow rate induced measurement error in flow-through nano-hole plasmonic sensor. Biomicrofluidics 9 (6), 064111.
Tu, Long, Li, Xuzhou, Wang, Wenhui, 2017. Label-free and real-time monitoring of single cell attachment on template-stripped plasmonic nano-holes. Sci. Reports 7 (1), 11020.
Najiminaini, M., et al., 2012. A three-dimensional plasmonic nanostructure with extraordinary optical transmission. Plasmonics 8 (2), 217–224.
Najiminaini, M., et al., 2010. Experimental and numerical analysis on the optical resonance transmission properties of nano-hole arrays. Opt. Express 18 (21), 22255–22270.
Xu, M., Obodo, D., Yadavalli, V.K., 2018. The design, fabrication, and applications of flexible biosensing devices–a review. Biosens. Bioelectron.
Stark, P.R., Halleck, A.E., Larson, D.N., 2005. Short order nanohole arrays in metals for highly sensitive probing of local indices of refraction as the basis for a highly multiplexed biosensor technology. Methods 37 (1), 37–47.
Singh, P., 2016. SPR biosensors: historical perspectives and current challenges. Sens. Actuators B: Chem. 229, 110–130.
Gordon, R., Sinton, D., Kavanagh, K.L., et al., 2008. A new generation of sensors based on extraordinary optical transmission. Acc. Chem. Res. 41 (8), 1049–1057.
Rodrigo, S.G., et al., 2009. Extraordinary optical transmission through hole arrays in optically thin metal films. Opt. Lett. 34 (1), 4–6.
Rodrigo, S.G., et al., 2010. Holes with very acute angles: a new paradigm of extraordinary optical transmission through strongly localized modes. Opt. Express 18 (23), 23691–23697.
Rodrigo, S.G., et al., 2008. Influence of material properties on extraordinary optical transmission through hole arrays. Phys. Rev. B Condens. Matter 77 (7), 075401–075401-8.
Vashist, S.K., et al., 2015. Emerging technologies for next-generation point-of-care testing. Trends Biotechnol. 33 (11), 692–705.
Chinnadayyala, S.R., et al., 2018. Recent advances in microfluidic paper-based electrochemiluminescence analytical devices for point-of-care testing applications. Biosens. Bioelectron.
Thio, T., et al., 2001. Enhanced light transmission through a single subwavelength aperture. Opt. Lett. 26 (24), 1972–1974.
Ebbesen, T.W., et al., 1998. Extraordinary optical transmission through sub-wavelength hole arrays. Nature 391 (6668), 667–669.
Zhang, T., et al., 2010. A nanostructured Fabry-Perot interferometer. Opt. Express 18 (19), 20282–20288.
Haynes, W.M., 2014. CRC Handbook of Chemistry and Physics. CRC press.
Li, X., et al., 2018. Single cell analysis: label-free optofluidic nanobiosensor enables real-time analysis of single-cell cytokine secretion. Small 14 (26), 1870119.